PCCP

ROYAL SOCIETY OF CHEMISTRY

PAPER

View Article Online
View Journal | View Issue

Cite this: *Phys. Chem. Chem. Phys.*, 2025, **27**, 18586

Tailoring ionic liquid properties *via* amino acid anions: structural influence of isoleucine, methionine, and serine anions†

Sonia Yadav and Anurag Prakash Sunda *

Choline amino acid ([Ch][AA]) ionic liquids have recently gained considerable attention due to their biocompatibility, low toxicity, and structural tunability, which makes them promising electrolytes for sustainable applications in electrochemistry. In the present study, classical molecular dynamics (MD) simulations were carried out to investigate the structural and dynamical behaviour of three choline-based amino acids ILs [Ch][Ile], [Ch][Met], and [Ch][Ser] at 300 K. Atomic charges are derived using density functional theory (DFT) calculations using the density derived electrostatic and chemical (DDEC) method. Radial distribution functions (RDFs) helped to probe the role of the carboxylate group and amino group in the local structural organisation, and electrostatic interactions were found to be dominant for the carboxylate group. The hydroxyl group in $[Ser]^-$ anions shows strong hydrogen bonding interaction with the $[Ch]^+$ cation's hydroxyl group. Spatial distribution function (SDF) analysis revealed the preferential hydrogen bonding patterns between the $[Ch]^+$ cation's tail and the amino acid anions. Structure factor is explored to obtain real-space correlation lengths and validate amino acid-driven experimental reported structural features of pre-peaks and molecular peaks. The mean square displacement plot is computed to calculate diffusion coefficients, and anionic mobility is found to be very similar for all three anions. However, there is a significant effect of counter amino acid anions on cationic mobility and the [Ch][Ser] IL exhibits the highest cation diffusion.

Received 26th May 2025,
Accepted 12th July 2025

DOI: 10.1039/d5cp01985k

rsc.li/pccp

1 Introduction

The rapid growth of the global population and the increasing reliance on electronic devices have significantly expanded the focus of energy sustainability. Over the past four decades, substantial research has been directed towards developing advanced energy materials and devices. Establishing eco-friendly power generation methods and the use of sustainable electrolyte technologies has become key to meet industrial and transportation needs. The overuse of fossil fuels and traditional organic solvents has led to adverse environmental impacts and health risks, emphasising the need for cleaner, alternative solutions.[1–3] Research focuses on batteries and fuel cell devices,[4,5] enhancing the design of hybrid materials and smart technologies. In parallel, emerging technologies are leading to new challenges regarding the extensive use of chemicals. This has now been critically reviewed by environmentalists due to the adverse effects of chemicals and hybrid materials. To find new ways to protect the environment and to address the accumulation of chemical waste from electronic devices, efficient and eco-friendly materials are in great demand in the energy sector. Apart from high energy efficiency and low emissions, factors such as the stability, cost, and durability of energy materials, remain the focus towards smart energy electrolyte materials.[6–8]

In the last few decades, the advancement in ionic liquids (ILs) has made substantial progress to revolutionise the electrolyte field of PEMFCs, super-capacitors and batteries. ILs have high ionic conductivity, high oxygen solubility, low toxicity, low vapour pressure, and can be tuned as needed.[9–13] They are widely used in various fields, including the treatment of biomass, the capture of acid gases, Li-ion batteries, and supercapacitors.[7,14] Protic ionic liquids are an interesting subclass of ILs and are known for improved electrolyte behaviour.[15,16] ILs exhibit complex structural and dynamic behaviour, and the size of constituent ions, effective charges, nano-segregation phenomena, and the presence of a hydrogen bonding network, are key factors to specify their characteristics.[17–19] Moreover, the structural

Department of Chemistry, J. C. Bose University of Science and Technology, YMCA Faridabad-121006, India. E-mail: anurag.sunda@gmail.com, anurag@jcboseust.ac.in

† Electronic supplementary information (ESI) available: DDEC6 partial charges are given in Tables S1–S3. Coordination numbers are provided in Table S4. Density fluctuations, log MSD with log time plot and its first derivative plot with time plot are shown in Fig. S1–S3, respectively. See DOI: **https://doi.org/10.1039/d5cp01985k**

isomerism, tail length of alkyl, and counterion's nature also affect the stability of ionic liquids and their dynamic properties.[20] Luo and coworkers[21,22] obtained a variety of physicochemical properties of IL electrolytes by preparing a non-stoichiometric electrolyte mixture with the help of an excess amount of counterion acid/base. Recently, Dagar *et al.*[23] highlighted molecular insights on the structural characteristics of composition-driven non-stoichiometric electrolytes using 1,2,4-triazolium methanesulfonate IL in methanesulfonic acid as the electrolyte.

The emphasis on ILs as green solvents further spurred interest in them to address eco-friendliness[24] and sustainability in electrolytes.[25–28] Tremendous efforts have been made to reduce chemical toxicity and improve sustainability by introducing biodegradable constituents.[29–32] With this objective, the synthesis aspect is revisited by replacing inorganic anions such as chloride, bromide, nitrate, triflate, SCN, and bistriflimide (TFSI) with amino acids.[33,34] Moreover, the counter-ions are replaced with biodegradable choline or betaine.[35–38] Choline refers to a class of quaternary ammonium salts often associated with an undefined counter anion (X^-), such as chloride, hydroxide, or tartrate; one of the most significant biodegradable, inexpensive, and water-soluble organic salts, is scientifically known as 2-hydroxyethyltrimethyl ammonium chloride.[39] Choline-based amino acid ILs ([Ch][AA]) can be designed using choline chloride ([Ch]Cl) as a cation source and amino acids to form their counter anions. These ionic liquids offer a range of applications in electrochemistry, supercapacitors, gas absorption, and as green catalysts in industrial and pharmaceutical chemistry.[40–43] Tao *et al.*[44] synthesized [Ch][Gly], [Ch][L-Ala], [Ch][β-Ala], [Ch][Pro], and [Ch][Ser] ILs and studied their physiochemical properties, ionic conductivity, refractive index, viscosity, thermal stability and density. Dhattarwal and Kashyap[45,46] explored intermediate range ordering, heterogeneity and side chain clusters in cholinium amino acid-based ILs. Campetella *et al.*[47] performed experimental and simulation studies on choline-based amino acid such as [Ch][Val], [Ch][Nva], [Ch][Leu] and [Ch][Nle] at the molecular level and emphasised how hydrogen bonds shape the local geometric structure. Chen *et al.*[48] demonstrated [Ch][AA] microstructural changes in their varying hydrated mixtures using lysine and aspartic acid amino acid anions. Miao *et al.*[42] reviewed task-specific ILs, and the authors emphasised hydrogen bond networks in cholinium phenylalaninate bio-IL, which lead to anion side chain segregation. Wong and coworkers[49] showed the nanostructure of [Ch][AA] IL aqueous mixtures using arginate and lysinate AA with the help of neutron diffraction, and found that the ion–dipole interactions dominate in their local liquid structure. Dong and co-workers explored the hydrogen bonding interaction in amino acid-based ILs.[50] To study the potential of [Ch][AA] ILs for various applications in the chemical industry, numerous researchers are involved in exploring these electrolytes for their unique physical properties.[51–56]

In this work, we aim to explore the structure–property relationship of choline-based [Ch][AA] ILs at 300 K using cholinium isoleucinate ([Ch][Ile]), and cholinium methionate ([Ch][Met]) and cholinium serinate ([Ch][Ser]). The chemical structure of choline-based amino acid ionic liquids is shown in Fig. 1. Density functional theory (DFT) and classical molecular

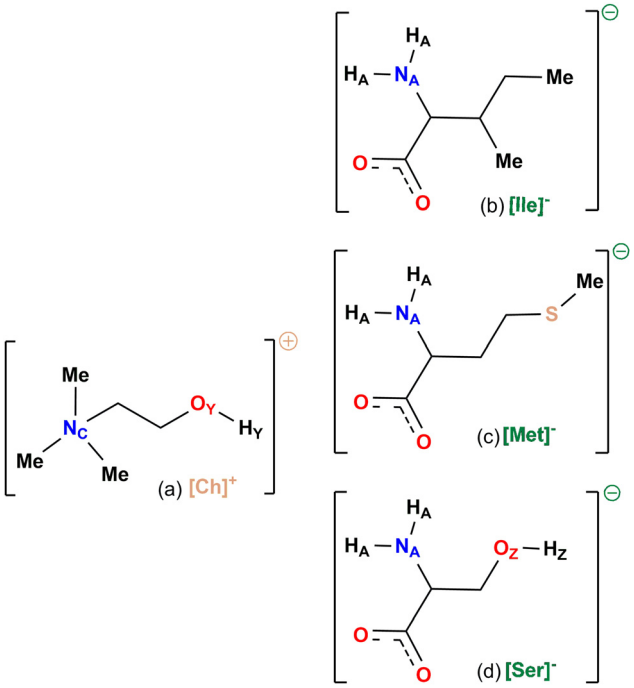

Fig. 1 The chemical structure of cholinium ($[Ch]^+$), isoleucinate ($[Ile]^-$), methionate ($[Met]^-$), and serinate ($[Ser]^-$).

dynamics (MD) simulations were employed to unveil characteristics of these ILs by analyzing binding energy, radial distribution function (RDF), structure factor, and spatial distribution and ion dynamics through mean square displacement (MSD), and velocity autocorrelation function (VACF). The analysis of structure–property relationships obtained from the MD simulation trajectory at 300 K is presented in the results and discussion section.

2 Computational and simulation details

2.1 DFT calculations

The initial configurations of $[Ch]^+$ cation, $[Ser]^-$, $[Ile]^-$, and $[Met]^-$ anions were generated utilizing Gaussian 16 software.[57] The geometry was optimized of an individual single ion-pair to their lowest energy states using CP2K-2022.1 software.[58] The Perdew, Burke, and Ernzerhof (PBE) exchange–correlation functional was utilized in the calculation.[59] The effect of the core electrons and nuclei on the valence electrons was observed with Geodecker–Teter–Hutter (GTH) pseudopotentials.[60] To describe the valence electrons, a triple-ζ basis set with double polarization functions and an energy cutoff of 280 Ry was used. The electron density corresponding to the optimized geometry was generated in the form of a cube file. DDEC6[61] method was used to obtain atomic charges by implementing the CHARGEMOL program and the calculated atomic charges are listed in the Tables S1–S3 of ESI.† The total net charge on each ion (cation or anion) were found to be less than unity and are mentioned in Table 1.

Table 1 Total ionic charge, system size (total number of atoms), and average density (ρ) obtained from 20 ns equilibration runs for the [Ch][Ile], [Ch][Met], and [Ch][Ser] ILs at 300 K respectively

Ionic liquid	Ionic charge	System size	Cubic box length (Å)	Density (g cm^{-3})	Exp. density (g cm^{-3})
[Ch][Ile]	±0.97	10 752	46.97	1.029	1.071 [62]
[Ch][Met]	±0.85	10 240	46.03	1.099	1.144 [62]
[Ch][Ser]	±0.90	8704	42.63	1.142	1.201,[44] 1.191 [62]

2.2 Simulation details

The MD simulations were performed for [Ch][Ile] IL, [Ch][Met] IL and [Ch][Ser] IL using GROMACS 2023.1 software[63] at 300 K for a system size consisting of 256 ion pairs. The initial input configurations were set by Packmol software.[64] Force field parameters for Choline cation except dihedrals were taken from OPLS[65] and dihedral angles were taken from the calculation reported by Sambasivaro *et al.*[66] Force field parameters for amino acids based anions [Ile] anion, [Ser] anion and [Met] anion were taken from the OPLS force field. Particle–mesh Ewald method (PME) method[67,68] used for the calculation of long-range electrostatic interactions. A distance cutoff of 1.2 nm was employed to calculate the pairwise interactions. The energy minimization was done by using the Steepest-Descent method. The equations of motion were integrated using the velocity Verlet algorithm with a time step of 1 femtosecond.

In all MD simulations, a cutoff distance of 1.2 nm was selected for non-bonded interactions. Each system was equilibrated for 20 ns using the NPT ensemble with a 1 bar isotropic pressure and mttk barostat. Temperature was kept constant using a Nose–Hoover thermostat with a coupling time of 0.2 ps.[69,70] The average density of [Ch][Ile], [Ch][Met], and [Ch][Ser] ILs calculated from a 20 ns equilibration run are provided in Table 1 and found to be in close agreement with the experimental values.[44,62] Fluctuations in the density profile are shown in Fig. S1 of the ESI.† Equilibration was followed by a 40 ns production run using the NVT ensemble. The final configurations from the NVT production run are depicted in Fig. 2 for [Ch][Ile], [Ch][Met], and [Ch][Ser] ILs, respectively. The production run trajectories were used to calculate the structural and dynamical properties of the ILs.

3 Results and discussion

3.1 Binding energy

The binding energies of ionic liquids were computed using DFT. The binding energy (E_{BE}) of each IL is determined using the total electronic energies of the ion pair and its constituent ions, according to the following expression:

$$E_{BE} = E_{IL} - (E_{Ch\ Cation} + E_{AA\ Anion})$$

where E_{IL}, E_{cation} and E_{anion} represent the energy of the isolated ion pair, cation and anion respectively. For each IL, four sets of single ion pairs are isolated from the production run configuration and the binding energy is averaged out of all four sets. The computed binding energies are as follows [Ch][Ile]: −43.91 kcal mol^{-1}, [Ch][Met]: −40.47 kcal mol^{-1} and [Ch][Ser]: −45.18 kcal mol^{-1}, respectively. Based on these binding energies, the relative ionic interaction strength among these ILs decreases as follows [Ch][Ser] IL > [Ch][Ile] IL > [Ch][Met] IL. The role of atomic interactions in these ILs is further examined using radial distribution functions (RDFs).

3.2 Radial distribution function

The strength of interionic atomic interactions and their characteristics significantly influence the properties of ILs. To explore these interactions, we analyzed various atom–atom RDFs, particularly focusing on cation–cation, anion–anion, cation–anions and hydrogen-bonding interactions. The RDF[71] $g_{AB}(r)$ between particles of different types can be given as:

$$g_{AB}(r) = \frac{1}{\langle \rho_B \rangle} \frac{1}{N_A} \sum_{i \in A}^{N_A} \sum_{j \in B}^{N_B} \frac{\delta(r_{ij} - r)}{4\pi r^2 dr} \quad (1)$$

where $\langle \rho_B \rangle$ is the bulk density of atom B averaged over all spheres

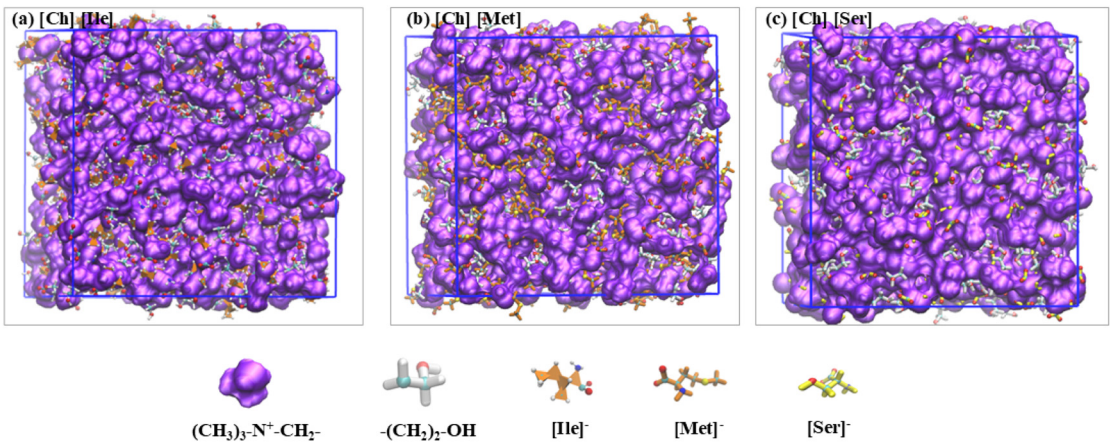

Fig. 2 Snapshots of the final configuration obtained from a 40 ns production run for (a) [Ch][Ile], (b) [Ch][Met], and (c) [Ch][Ser] ILs, respectively. [Color scheme: (i) [Ch]$^+$ cation with quaternary $(CH_3)_3NCH_2$ group and –(CH_2)–O–H surface, Licorice & CPK; (ii) [Ile]$^-$ anion, Licorice & CPK; (iii) [Met]$^-$ anion, Licorice & CPK; (iv) [Ser]$^-$ anion, Licorice & CPK. (C-atom: cyan, N-atom: blue, O-atom: red, H-atom: white, S-atom: yellow)].

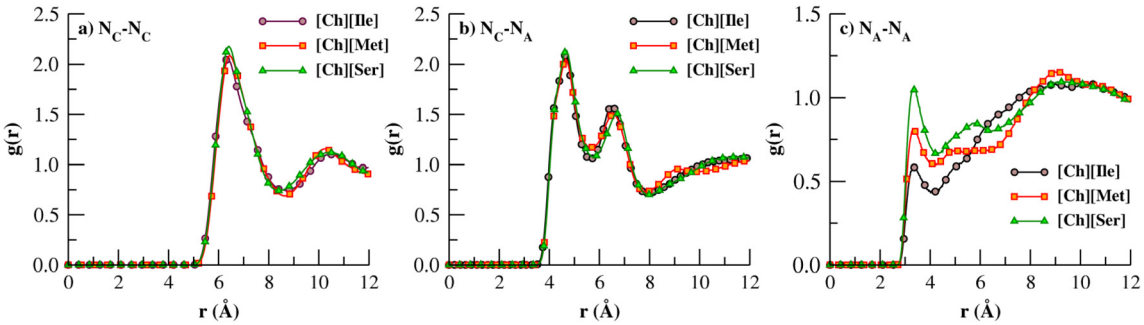

Fig. 3 RDF for (a) cation–cation (N_C–N_C), (b) cation–anion (N_C–N_A), (c) anion–anion (N_A–N_A), interactions in [Ch][Ile], [Ch][Met], and [Ch][Ser] ILs at 300 K.

around atom A. The atomic description for RDF analysis is given in Fig. 1 as subscript notation.

Inter-atomic interactions between ions are examined by computing N_C–N_C RDF for nitrogen atoms and are shown in Fig. 3. The cation–cation interactions in Fig. 3a for $[Ch]^+$ ions depict strong interactions between quaternary heads with a distinguishing peak at 6.3 Å. The RDF profile shows a good overlap for all three ILs with a slightly intense peak for [Ch][Ser] IL. A similar overlap RDF profile is obtained for cation–anion interactions between the quaternary nitrogen atom and amino acid nitrogen atom and is shown in (Fig. 3b). However, the peak is found to be bifurcated with two distinct interactions at 4.6 Å and 6.5 Å, respectively. The anion–anion interactions between NH_2-groups are found to be relatively weak (Fig. 3c) compared to cation–cation and cation–anion interactions. The N_A–N_A RDF peak at 3.2 Å shows that the interaction between $[Ser]^-$ anions are more significant than the $[Ile]^-$ and $[Met]^-$ anions. A similar observation is seen at higher coordinator number for $[Ser]^-$ anions as provided in Table S4 of ESI.†

Further, the oxygen–oxygen atom interactions are calculated between the ions to explore the role of carboxylate groups of amino acids. The O–O RDF profile for interactions between the carboxylate groups is shown in Fig. 4a and the broad RDF profile peak at 4 to 10 Å signifies very weak interactions. However, the O–O_Y RDF distinguish the very strong interactions of carboxylate group oxygen atoms with $[Ch]^+$ cation hydroxyl tail. A sharp peak at 2.8 Å in Fig. 4b indicates hydrogen bonding interactions between the $[Ch]^+$ cations and carboxylate group of amino acid anions. The RDF peak at 4.5 Å with a small shoulder at 5.8 Å is obtained for interactions between the oxygen atom of carboxylate groups and the nitrogen atom of $[Ch]^+$ cations (see Fig. 4c). It suggest that electrostatic interactions configure anions at around 4–5 Å from the quaternary heads of the $[Ch]^+$ cations. Moreover, the O–N_C interactions are relatively weaker in [Ch][Ser] compared to [Ch][Ile] and [Ch][Met] ILs, and are also reflected in the coordination number.

To understand the role of the amino group of anions in cation–anion interactions, the H_Y–N_A and H_A–O_Y RDFs are calculated and are shown in Fig. 5. The $[Ch]^+$ cation tail hydrogen atom and amino group nitrogen atom interactions are found to be similar in all three ILs except for a small kink at 2 Å in [Ch][Met] (a typical hydrogen bonding distance for N···H). The hydrogen bonding interactions between the cationic tail oxygen atoms and amino group hydrogens are found to be insignificant (see Fig. 5b) which reveals that the cationic hydroxyl tail hydrogen bonding interactions are dominated by electrostatic interactions. To gain more insight, we calculated the average number of hydrogen bonds per ion-pair for these interactions, provided in Table S5 of ESI.† The average number of hydrogen bonds per ion pair for the cationic hydroxyl tail and $-NH_2$ group is found to be near to zero, which is in agreement with the RDF results. Moreover, the H_A–N_C RDF between the hydrogen atom of the amino group and quaternary nitrogen atom of $[Ch]^+$ heads, show a peak profile in line with

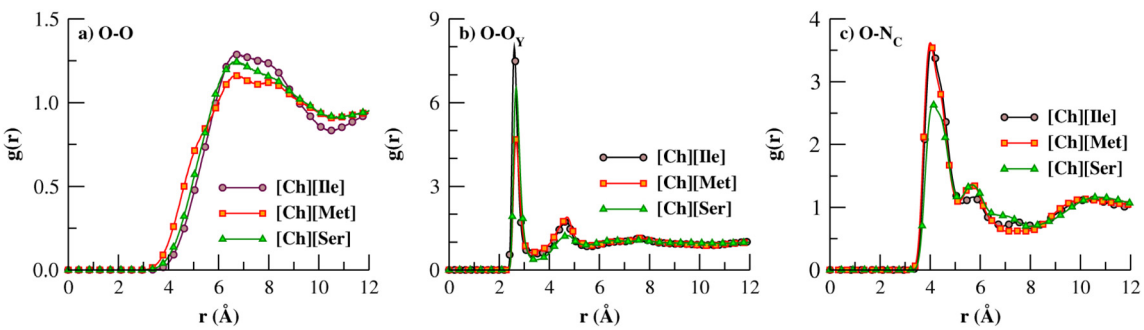

Fig. 4 RDF for oxygen–oxygen atom interactions between (a) carboxylate groups of anions (O–O), (b) carboxylate group and $[Ch]^+$ cation (O–O_Y); (c) RDF for oxygen–nitrogen atom interactions, between the carboxylate groups of anions and $[Ch]^+$ cation (O–N_C) in [Ch][Ile], [Ch][Met], and [Ch][Ser] ILs, respectively.

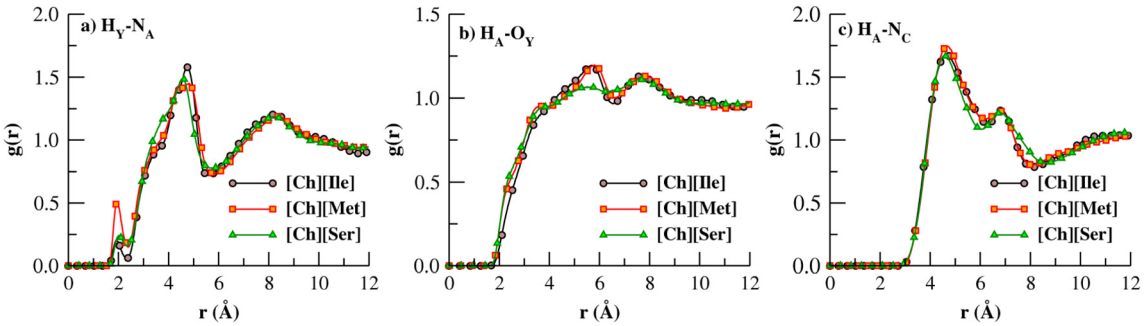

Fig. 5 The RDF derived from 40 ns NVT ensemble simulation for (a) H_Y–N_A, (b) H_A–O_Y, (c) H_A–N_C, interactions of [Ch][Ile], [Ch][Met] and [Ch][Ser] ILs, at 300 K.

cation–anion interactions. In Fig. 5c interactions were seen at 4.5 Å with a shoulder at 7 Å in the RDF peak.

To summarise the RDF analysis, the major interactions in $[Ch]^+$ cations and amino acids are governed by electrostatic attraction between quaternary heads and amino acid anions, and these interactions are stronger in $[Ser]^-$ anions compared to the $[Ile]^-$ and $[Met]^-$ anions. The hydroxyl group of the $[Ch]^+$ cationic tail shows significant hydrogen bonding interactions with the carboxylate group of amino acid anions. This behaviour is further characterized through spatial correlations between ions.

3.3 Spatial distribution function

To interpret the three-dimensional structural features of [Ch][AA] ILs, the spatial distribution is examined for hydrogen (H atoms), and oxygen (O atoms) of $[Ch]^+$ cations (hydroxyl tail) around the $[Ile]^-$, $[Met]^-$, and $[Ser]^-$ anions using Travis.[72] For all three ILs, the spatial distribution density for the oxygen atom is depicted in red and the hydrogen atom in white around the anions (see Fig. 6). The spatial density distribution map differentiates the structural signatures of $[Ile]^-$ and $[Met]^-$ and $[Ser]^-$ anions. Similar to RDF observations, the distribution of the cationic tail is found to be around the carboxylate group of amino acids. In the case of $[Ile]^-$ anions, the density maps show an overlap for oxygen and hydrogen atom distribution (Fig. 6a) which is more distinct in $[Met]^-$ and $[Ser]^-$ anions. Moreover, a significant distribution density map extension is seen around the hydroxyl group in $[Ser]^-$ anions. It clearly shows that strong hydrogen bonding prevails between the hydroxyl groups of the cations and anions in [Ch][Ser] ILs. Among the three ILs, [Ch][Ser] demonstrates the most pronounced hydrogen bonding network due to the additional hydroxyl group in the $[Ser]^-$ anions.

3.4 X-ray scattering structure factor

The X-ray scattering structure factor is calculated using $g(r)$ and the expression[71] is given below such as:

$$S_{ij}(q) = 4\pi\rho_0 \int_0^{r_{max}} r^2 [g_{ij}(r) - 1] \frac{\sin(qr_{ij})}{qr_{ij}} dr \qquad (2)$$

where $S_{ij}(q)$ is the partial structure factor, defined in terms of an integral transformation of the RDF $g(r)$, ρ_0 is atomic density, r_{max} is half the box length of the simulation box to minimize periodic boundary effects. The total structure factor is calculated for all three ILs as described previously[45] and shown in Fig. 7.

For all three ILs, a principal peak is obtained in the structure factor profile within the range 1.35–1.48 $Å^{-1}$. This peak represents structural correlations arising from inter molecular and intra molecular nearest-neighbor interactions. The featured

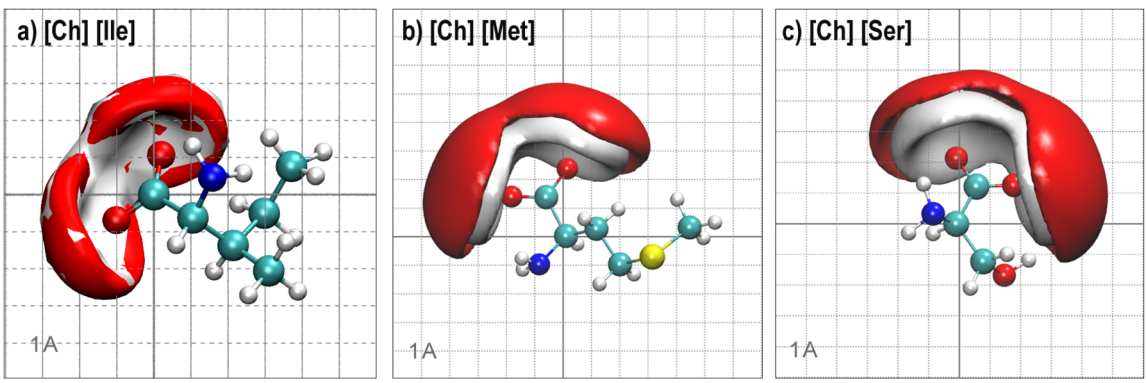

Fig. 6 Spatial distribution density maps calculated for the distribution of oxygen (O) and hydrogen (H) atoms of $[Ch]^+$ cations around the (a) $[Ile]^-$ anion, (b) $[Met]^-$ anion and (c) $[Ser]^-$ anions. [Color scheme anions (CPK): C-cyan, O-red, N-blue, S-yellow, H-white; iso-surface of $[Ch]^+$ cations: O-red, and H-white at isovalue 0.006 $Å^3$.]

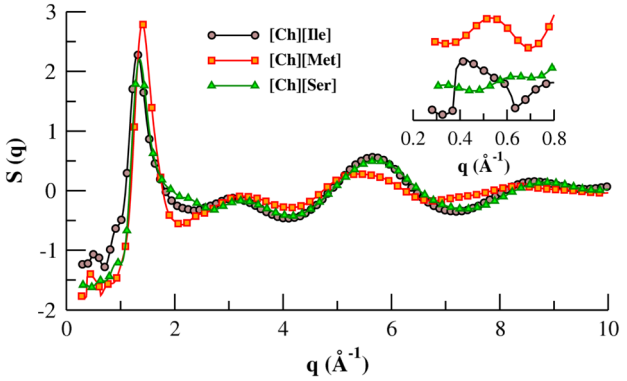

Fig. 7 The total X-ray scattering structure function $S(q)$ calculated for [Ch][Ile], [Ch][Met], and [Ch][Ser] ILs at 300 K.

peak for the structure factor profile in the context of amino acids at 0.55 Å^{-1} for [Ch][Ile] and 0.40 Å^{-1} for [Ch][Met] ILs, is considered as a pre-peak (see inset of Fig. 7). This peak is associated with real-space correlation lengths of 11.4 Å and 15.7 Å and signifies the presence of intermediate-range ordering (IRO) in these ILs. These findings are in close agreement with the [Ch][Met] IL in an earlier study[45] on the structure factor profile. However, there is no such pre-peak profile seen in the [Ch][Ser] IL and this is consistent with experiments.[73] Furthermore, the molecular peak observed at 3.1 Å^{-1} reflects an effective direct-space correlation length of 2.0 Å. This suggests strong cation–anion interactions which might be facilitated by hydrogen bonding and this arises due to relatively short distance intermolecular interactions. These characteristics of structure factor profiles in [Ch][AA] depict the conformational equilibrium inherent to the molecular structure.

3.5 Velocity autocorrelation function

The velocity autocorrelation function (VACF) for cation–cation and anion–anion interactions is calculated to capture insights into the microscopic dynamics and to the caging of ions. For the VACF calculation, a 1 ns NVT trajectory was generated at 300 K using a 1 fs time step where the output coordinates are recorded at 10 fs intervals. The center-of-mass VACF is computed between $[Ch]^+$–$[Ch]^+$ cations ($[Ch]^+$) and between the anions such as $[Ile]^-$–$[Ile]^-$, $[Met]^-$–$[Met]^-$, and $[Ser]^-$–$[Ser]^-$ using eqn (3):[74]

$$C_v(t) = \langle \vec{v}(0)\cdot\vec{v}(t)\rangle \quad (3)$$

Fig. 8 shows that the depth of VACF for cations in [Ch][Ile] and [Ch][Met] Ils overlap each other and there is a small increase in depth for the edge of the [Ch][Ser] IL. The first minimum in the VACF for the $[Ch]^+$–$[Ch]^+$ cations is relatively more pronounced compared to anion–anion VACFs. This suggest that cage effects and local structural ordering for the cations is relatively stronger compared to the anions. Moreover, the VACF decay profile of the $[Ile]^-$ and $[Met]^-$ anions show substantial similarity. There is a slightly deeper decay profile observed in the case of $[Ser]^-$ anions with a relatively shorter time scale which corroborates with the higher binding energy and higher possibility of hydrogen boding interactions due to hydroxyl groups in $[Ser]^-$ anions.

3.6 Ionic mobility

To investigate the ionic mobility of [Ch][AA] ILs, the mean squared displacement (MSD) plot with time is obtained from 40 ns production using the Einstein relation[74] (see eqn (4)).

$$D_A = \frac{1}{6t}\lim_{t\to\infty}\langle \|\mathbf{r}(t) - \mathbf{r}_0\|^2\rangle \quad (4)$$

The calculated MSD plots for $[Ch]^+$ cations and anions in [Ch][Ile], [Ch][Met], and [Ch][Ser] ILs are shown in Fig. 9. To calculate the diffusion coefficients from the linear regime of the MSD plot, the slope of the log–log plot of MSD with time is examined (Fig. S2 in the ESI†) and found to be ~1 for the 4 ns to 36 ns time regime. The time-dependent $\beta(t)$ plot ($\beta(t) = d\log(\text{MSD})/d\log(t)$) r[75] between 4 ns to 36 ns indicates diffusive behavior with a $\beta(t)$ value around unity as shown in Fig. S3 in the ESI.† The calculated diffusion coefficients from the linear regime for cations and anions are provided in Table 2. The mobility of $[Ch]^+$ cations is increased by a factor of 1.22 for the [Ch][Met] IL and increased by a factor of 1.44 for the [Ch][Ser] IL, with respect to the [Ch][Ile] IL. The diffusion of $[Ile]^-$, $[Met]^-$, and $[Ser]^-$ anions is found to be similar. As expected, the mobility of cation and anions in [Ch][Ser] ILs is found to be the highest among all three ILs. Further, cation–anion

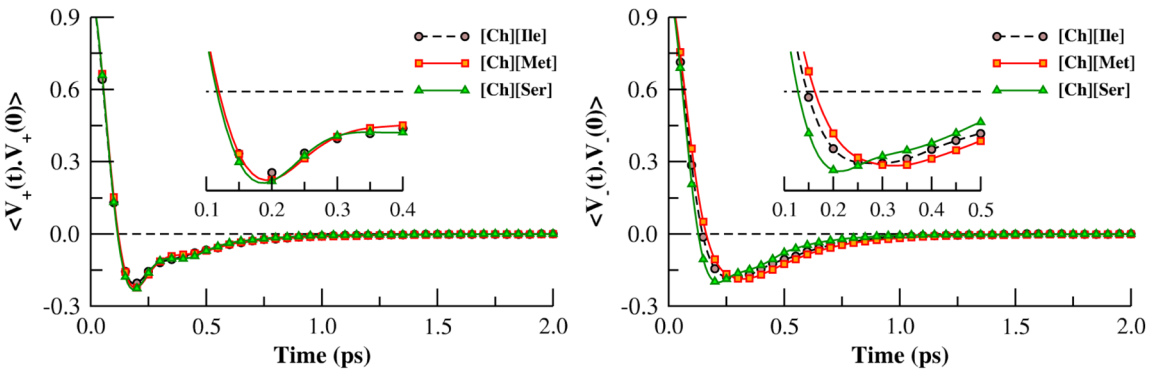

Fig. 8 The velocity autocorrelation function derived from a 40 ns NVT ensemble simulation for [Ch][Ile] IL, [Ch][Met] and [Ch][Ser] ILs at 300 K.

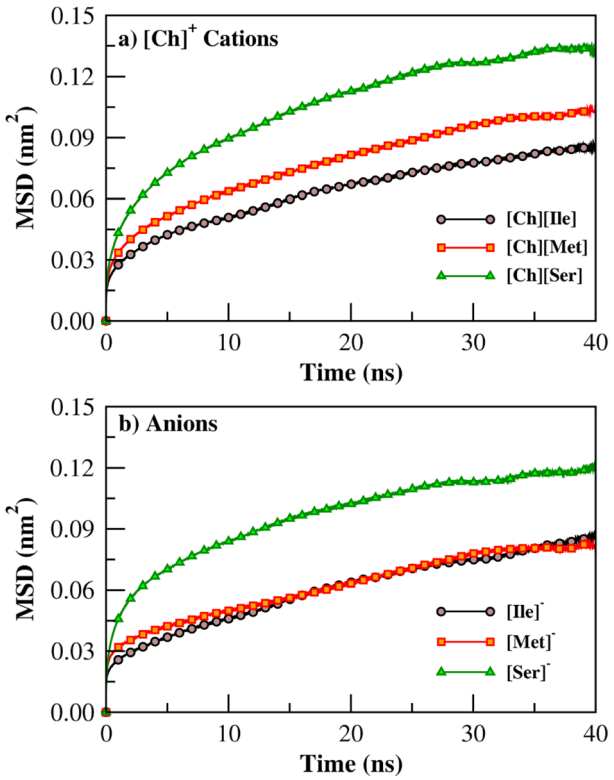

Fig. 9 MSD plot with time computed from 40 ns production runs for (a) $[Ch]^+$ cation, and (b) for amino acid anions in [Ch][Ile], [Ch][Met], and [Ch][Ser] ILs.

Table 2 Diffusion coefficients ($D \times 10^{-8}$ cm^2 s^{-1}) and Nernst–Einstein conductivity (σ_{N-E} in μS cm^{-1}) calculated from 40 ns production runs

IL	D_+	D_-	σ_{N-E}	$\sigma_{Exp.}$
[Ch][Ile]	0.2198 ± 0.04	0.2405 ± 0.04	71.62	10.61[62]
[Ch][Met]	0.2703 ± 0.03	0.2236 ± 0.02	58.70	42.69[62]
[Ch][Ser]	0.3172 ± 0.01	0.2503 ± 0.01	94.71	9.3,[44] 17.46[62]

diffusion coefficients are used to compute the Nernst–Einstein ionic conductivity[76,77] (σ_{N-E}) using eqn (5) such as

$$\sigma_{N-E} = \frac{e^2}{Vk_BT}\left(n_+ z_+^2 D_+ + n_- z_-^2 D_-\right) \quad (5)$$

where n_+ and n_- are the number of cation and anions, z_+ and z_- are the charges on the cation and anions, respectively, in ILs. The calculated values are provided in Table 2 and compared with experimental conductivity. The σ_{N-E} from simulations overestimates the conductivity and there is significant deviation in the calculated values with experiment. As independent ionic mobility is expected for σ_{N-E} calculations and such overestimation re-affirms the limitation[78] of σ_{N-E} towards ion pairing correlations such as that seen in [Ch][AA] ILs.

4 Conclusions

In this work, molecular insights are explored using molecular dynamics tools for [Ch][AA] ILs at 300 K by analyzing RDFs, spatial distribution functions, structure factors, VACFs, MSD *etc.* The computed average densities closely resemble experimental results for the [Ch][Ile] IL, [Ch][Met] IL and [Ch][Ser] IL. Among all three ILs, the calculated binding energy is found to be the highest for [Ch][Ser] IL. The RDF results offer detailed insights into the local coordination environment, particularly highlighting the strong electrostatic interactions between the quaternary N-atom of $[Ch]^+$ cations and amino acid anions. The carboxylate group exhibits significant hydrogen bonding with the $[Ch]^+$ cation hydroxyl tail. The presence of the hydroxyl group in the $[Ser]^-$ anion further strengthens these hydrogen bonding interactions. Spatial density distribution maps reveal the extended distribution of the carboxylate group around the $[Ch]^+$ cationic tail. Both ion–ion interactions and hydrogen bonding interactions are validated through structure factor profiles. Results are found to be in close agreement with experiments and with previous simulation results on amino acids. The effect of amino acid anions on counter ion $[Ch]^+$ cation mobility is observed and hydrogen bonding interactions may play a significant role in further fine-tuning of the electrolyte ionic mobility. Overestimation of the Nernst–Einstein conductivity highlights the presence of ion pairing and correlated motion. In summary, this work attempts to screen the effect of amino acids as anions on green systems consisting of $[Ch]^+$ cations and develops an understanding of quaternary heads and tails in recognition of ion-paring of biocompatible electrolyte systems.

Author contributions

SY performed all the calculations and carried out the formal analysis. APS administrated the project and helped in the funding acquisition, formal analysis and investigation. All authors equally contributed to writing and review – editing.

Conflicts of interest

There are no conflicts to declare.

Data availability

The data supporting this article have been included as part of the ESI.†

Acknowledgements

APS acknowledges the Anusandhan National Research Foundation (ANRF) for the SERB – CRG/2022/001938 Grant.

Notes and references

1 M. Mirzaei-Saatlo, E. Asghari and H. Shekaari, *J. Energy Storage*, 2025, **108**, 115069.
2 G. de Araujo Lima e Souza, M. E. di Pietro, F. Castiglione, P. Fazzio Martins Martinez, C. C. Fraenza, P. Stallworth,

S. Greenbaum, A. Triolo, G. Battista Appetecchi and A. Mele, *Electrochim. Acta*, 2024, **474**, 143466.
3 S. Brahma, J. Huddleston and A. Lahiri, *ChemElectroChem*, 2024, **11**, e202400511.
4 Y. Wang, Y. Pang, H. Xu, A. Martinez and K. S. Chen, *Energy Environ. Sci.*, 2022, **15**, 2288–2328.
5 K. Sau, S. Takagi, T. Ikeshoji, K. Kisu, R. Sato, E. C. dos Santos, H. Li, R. Mohtadi and S.-I. Orimo, *Commun. Mater.*, 2024, **5**, 122.
6 F. Van Der Linden, E. Pahon, S. Morando and D. Bouquain, *J. Power Sources*, 2023, **575**, 233168.
7 Q. Liu, H. Liu, W. Zhang, Q. Ma, Q. Xu, K. Hooshyari and H. Su, *Chem. – Eur. J.*, 2024, **30**, e202303525.
8 Z. Xie, J. Wang, G. Zhao, Q. Zhang, H. Fan, A. Zeng and W. Ding, *Catal. Sci. Technol.*, 2024, **14**, 4420–4431.
9 A. Mondal and A. P. Sunda, *Phys. Chem. Chem. Phys.*, 2018, **20**, 19268–19275.
10 A. Mondal and S. Balasubramanian, *J. Phys. Chem. B*, 2014, **118**, 3409–3422.
11 K. Matuszek, S. L. Piper, A. Brzeczek-Szafran, B. Roy, S. Saher, J. M. Pringle and D. R. MacFarlane, *Adv. Mater.*, 2024, **36**, 2313023.
12 C. Wang, J.-j Zhu, Y. Qiu, H. Wang, Y. Xu, H. Haghani and H. Er, *J. Solution Chem.*, 2025, **54**, 55–72.
13 Q. Li, J. Jiang, G. Li, W. Zhao, X. Zhao and T. Mu, *Sci. China: Chem.*, 2016, **59**, 571–577.
14 E. Piatti, L. Guglielmero, G. Tofani, A. Mezzetta, L. Guazzelli, F. D'Andrea, S. Roddaro and C. Pomelli, *J. Mol. Liq.*, 2022, **364**, 120001.
15 G. de Araujo Lima e Souza, M. E. Di Pietro, F. Castiglione, P. Fazzio Martins Martinez, M. Middendorf, M. Schonhoff, C. C. Fraenza, P. Stallworth, S. Greenbaum, A. Triolo, G. B. Appetecchi and A. Mele, *Electrochim. Acta*, 2024, **475**, 143598.
16 T. Stettner and A. Balducci, *Energy Storage Mater.*, 2021, **40**, 402–414.
17 A. P. Sunda, A. Mondal and S. Balasubramanian, *Phys. Chem. Chem. Phys.*, 2015, **17**, 4625–4633.
18 M. Mirzaei-Saatlo, E. Asghari, H. Shekaari, B. Pollet and R. Vinodh, *Electrochim. Acta*, 2024, **474**, 143499.
19 J. Bailey, E. L. Byrne, P. Goodrich, P. Kavanagh and M. Swadzba-Kwasny, *Green Chem.*, 2024, **26**, 1092–1131.
20 M. Villanueva, P. Vallet, T. Teijeira, A. Santiago-Alonso, A. Amigo, E. Tojo, L. M. Varela, J. J. Parajó and J. Salgado, *J. Therm. Anal. Calorim.*, 2024, 1–11.
21 J. Luo, J. Hu, W. Saak, R. Beckhaus, G. Wittstock, I. F. J. Vankelecom, C. Agert and O. Conrad, *J. Mater. Chem.*, 2011, **21**, 10426–10436.
22 J. You, Q. Gong, S. Rohde, H. Zhang, C. Korte, B. Gollas and J. Luo, *J. Mol. Liq.*, 2024, **413**, 125663.
23 S. Dagar, S. Liu, J. Luo and A. P. Sunda, *J. Phys. Chem. B*, 2025, **129**, 338–347.
24 G.-H. Tao, L. He, W.-S. Liu, L. Xu, W. Xiong, T. Wang and Y. Kou, *Green Chem.*, 2006, **8**, 639–646.
25 S. Troger-Muller, J. Brandt, M. Antonietti and C. Liedel, *Chem. – Eur. J.*, 2017, **23**, 11810–11817.
26 S. Shahzad, A. Shah, E. Kowsari, F. J. Iftikhar, A. Nawab, B. Piro, M. S. Akhter, U. A. Rana and Y. Zou, *Global Challenges*, 2019, **3**, 1800023.
27 M. Pająk, K. Hubkowska, D. Monikowska, G. Lota and A. Czerwiński, *Energy Convers. Manage.: X*, 2023, **20**, 100500.
28 K. Vishweswariah, A. K. Madikere Raghunatha Reddy and K. Zaghib, Beyond Organic Electrolytes: An Analysis of Ionic Liquids for Advanced Lithium Rechargeable Batteries, *Batteries*, 2024, **10**, 436.
29 V. Beniwal and A. Kumar, *J. Phys. Chem. B*, 2017, **121**, 11367–11375.
30 K. Dong, X. Liu, H. Dong, X. Zhang and S. Zhang, *Chem. Rev.*, 2017, **117**, 6636–6695.
31 P. Ossowicz, J. Klebeko, B. Roman, E. Janus and Z. Rozwadowski, *Molecules*, 2019, **24**, 3252.
32 B. Kirchner, J. Blasius, V. Alizadeh, A. Gansäuer and O. Hollóczki, *J. Phys. Chem. B*, 2022, **126**, 766–777.
33 H. Ohno and K. Fukumoto, *Acc. Chem. Res.*, 2007, **40**, 1122–1129.
34 S. Kirchhecker and D. Esposito, *Curr. Opin. Green Sustainable Chem.*, 2016, **2**, 28–33.
35 Y. De Gaetano, A. Mohamadou, S. Boudesocque, J. Hubert, R. Plantier-Royon and L. Dupont, *J. Mol. Liq.*, 2015, **207**, 60–66.
36 P. Pavez, R. Figueroa, M. Medina, D. MillÃ¡n, R. D. Falcone and R. A. Tapia, *ACS Omega*, 2020, **5**, 26562–26572.
37 J. Chen, X. Zeng and L. Chen, *Phys. Chem. Chem. Phys.*, 2025, **27**, 5256–5270.
38 S. Yadav and A. P. Sunda, *ChemPhysChem*, 2025, **26**, e202500139.
39 B. L. Gadilohar and G. S. Shankarling, *J. Mol. Liq.*, 2017, **227**, 234–261.
40 S. Bhattacharyya and F. U. Shah, *J. Mol. Liq.*, 2018, **266**, 597–602.
41 A. Filippov, S. Bhattacharyya and F. U. Shah, *J. Mol. Liq.*, 2019, **276**, 748–752.
42 S. Miao, R. Atkin and G. Warr, *Green Chem.*, 2022, **24**, 7281–7304.
43 I. Jankowska, M. Bielejewski, P. Ławniczak, R. Pankiewicz and J. Tritt-Goc, *Cellulose*, 2023, **31**, 427–441.
44 D.-J. Tao, Z. Cheng, F.-F. Chen, Z.-M. Li, N. Hu and X.-S. Chen, *J. Chem. Eng. Data*, 2013, **58**, 1542–1548.
45 H. S. Dhattarwal and H. K. Kashyap, *Phys. Chem. Chem. Phys.*, 2021, **23**, 10662–10669.
46 H. S. Dhattarwal and H. K. Kashyap, *Chem. Rec.*, 2023, **23**, e202200295.
47 M. Campetella, A. Le Donne, M. Daniele, L. Gontrani, S. Lupi, E. Bodo and F. Leonelli, *J. Phys. Chem. B*, 2018, **122**, 2635–2645.
48 J. Chen, X. Zeng and L. Chen, *Phys. Chem. Chem. Phys.*, 2022, **24**, 17792–17808.
49 L. N. Wong, M. Brunner, S. Imberti, G. G. Warr and R. Atkin, *J. Phys. Chem. B*, 2024, **128**, 4853–4863.
50 W. Dong, P. R. Batista, J. Blasius and B. Kirchner, *Phys. Chem. Chem. Phys.*, 2025, **27**, 4457–4466.
51 A. Le Donne, H. Adenusi, F. Porcelli and E. Bodo, *J. Phys. Chem. B*, 2019, **123**, 5568–5576.

52 F. Elhi, H. Priks, P. Rinne, N. Kaldalu, E. Žusinaite, U. Johanson, A. Aabloo, T. Tamm and K. Põhako-Esko, *Smart Mater. Struct.*, 2020, **29**, 055021.
53 M. Moosavi, N. Banazadeh and M. Torkzadeh, *J. Phys. Chem. B*, 2019, **123**, 4070–4084.
54 G. Yang, S. Wang, Y. Yuan and J. Lin, *J. Phys. Chem. Solids*, 2024, **193**, 112181.
55 S. Russo and E. Bodo, *Molecules*, 2024, **29**, 1524.
56 A. Le Donne and E. Bodo, *Biophys. Rev.*, 2021, **13**, 147–160.
57 M. J. Frisch, G. W. Trucks, H. B. Schlegel, G. E. Scuseria, M. A. Robb, J. R. Cheeseman, G. Scalmani, V. Barone, G. A. Petersson, H. Nakatsuji, X. Li, M. Caricato, A. V. Marenich, J. Bloino, B. G. Janesko, R. Gomperts, B. Mennucci, H. P. Hratchian, J. V. Ortiz, A. F. Izmaylov, J. L. Sonnenberg, D. Williams-Young, F. Ding, F. Lipparini, F. Egidi, J. Goings, B. Peng, A. Petrone, T. Henderson, D. Ranasinghe, V. G. Zakrzewski, J. Gao, N. Rega, G. Zheng, W. Liang, M. Hada, M. Ehara, K. Toyota, R. Fukuda, J. Hasegawa, M. Ishida, T. Nakajima, Y. Honda, O. Kitao, H. Nakai, T. Vreven, K. Throssell, J. A. Montgomery, Jr., J. E. Peralta, F. Ogliaro, M. J. Bearpark, J. J. Heyd, E. N. Brothers, K. N. Kudin, V. N. Staroverov, T. A. Keith, R. Kobayashi, J. Normand, K. Raghavachari, A. P. Rendell, J. C. Burant, S. S. Iyengar, J. Tomasi, M. Cossi, J. M. Millam, M. Klene, C. Adamo, R. Cammi, J. W. Ochterski, R. L. Martin, K. Morokuma, O. Farkas, J. B. Foresman and D. J. Fox, *Gaussian~16 Revision C.01*, Gaussian Inc., Wallingford CT, 2016.
58 T. D. Kühne, M. Iannuzzi, M. D. Ben, V. V. Rybkin, P. Seewald, F. Stein, T. Laino, R. Z. Khaliullin, O. Schütt, F. Schiffmann, D. Golze, J. Wilhelm, S. Chulkov, M. H. Bani-Hashemian, V. Weber, U. Borštnik, M. Taillefumier, A. S. Jakobovits, A. Lazzaro, H. Pabst, T. Müller, R. Schade, M. Guidon, S. Andermatt, N. Holmberg, G. K. Schenter, A. Hehn, A. Bussy, F. Belleflamme, G. Tabacchi, A. Glöß, M. Lass, I. Bethune, C. J. Mundy, C. Plessl, M. Watkins, J. VandeVondele, M. Krack and J. Hutter, *J. Chem. Phys.*, 2020, **152**, 194103.
59 J. P. Perdew, K. Burke and M. Ernzerhof, *Phys. Rev. Lett.*, 1996, **77**, 3865.
60 S. Goedecker, M. Teter and J. Hutter, *Phys. Rev. B: Condens. Matter Mater. Phys.*, 1996, **54**, 1703.
61 N. G. Limas and T. A. Manz, *RSC Adv.*, 2018, **8**, 2678–2707.
62 S. De Santis, G. Masci, F. Casciotta, R. Caminiti, E. Scarpellini, M. Campetella and L. Gontrani, *Phys. Chem. Chem. Phys.*, 2015, **17**, 20687–20698.
63 M. Abraham, A. Alekseenko, C. Bergh, C. Blau, E. Briand, M. Doijade, S. Fleischmann, V. Gapsys, G. Garg, S. Gorelov, G. Gouaillardet, A. Gray, M. E. Irrgang, F. Jalalypour, J. Jordan, C. Junghans, P. Kanduri, S. Keller, C. Kutzner, J. A. Lemkul, M. Lundborg, P. Merz, V. Miletić, D. Morozov, S. Páll, R. Schulz, M. Shirts, A. Shvetsov, B. Soproni, D. van der Spoel, P. Turner, C. Uphoff, A. Villa, S. Wingbermühle, A. Zhmurov, P. Bauer, B. Hess and E. Lindahl, *GROMACS 2023.1 Source code*, 2023, DOI: **10.5281/zenodo.7852175**.
64 L. Martínez, R. Andrade, E. G. Birgin and J. M. Martínez, *J. Comput. Chem.*, 2009, **30**, 2157–2164.
65 W. L. Jorgensen, D. S. Maxwell and J. Tirado-Rives, *J. Am. Chem. Soc.*, 1996, **118**, 11225–11236.
66 S. V. Sambasivarao and O. Acevedo, *J. Chem. Theory Comput.*, 2009, **5**, 1038–1050.
67 T. Darden, D. York and L. Pedersen, *J. Chem. Phys.*, 1993, **98**, 10089–10092.
68 U. Essmann, L. Perera, M. L. Berkowitz, T. Darden, H. Lee and L. G. Pedersen, *J. Chem. Phys.*, 1995, **103**, 8577–8593.
69 S. Nosé, *J. Chem. Phys.*, 1984, **81**, 511–519.
70 W. G. Hoover, *Phys. Rev. A: At., Mol., Opt. Phys.*, 1985, **31**, 1695–1697.
71 J.-P. Hansen and I. R. McDonald, *Theory of Simple Liquids*, Academic Press, Oxford, 4th edn, 2013.
72 M. Brehm and B. Kirchner, *J. Chem. Inf. Model.*, 2011, **51**, 2007–2023.
73 L. Gontrani, *Biophys. Rev.*, 2018, **10**, 873–880.
74 M. Allen and D. Tildesley, *Computer Simulation of Liquids*, Clarendon Press, 1989.
75 E. W. J. Castner, C. J. Margulis and M. Maroncelli, *Annu. Rev. Phys. Chem.*, 2011, **62**, 85–105.
76 J. Newman and K. E. Thomas-Alyea, *Electrochemical Systems*, Wiley-Interscience, Hoboken, NJ, 3rd edn, 2004.
77 G. Feng, M. Chen, S. Bi, Z. A. H. Goodwin, E. B. Postnikov, N. Brilliantov, M. Urbakh and A. A. Kornyshev, *Phys. Rev. X*, 2019, **9**, 021024.
78 A. France-Lanord and J. C. Grossman, *Phys. Rev. Lett.*, 2019, **122**, 136001.

